Shot-noise limited phase-sensitive imaging of moving samples by phase-restoring subpixel motion correction in Fourier-domain optical coherence tomography

Huakun Li[1], Bingyao Tan[1-3], Vimal Prabhu Pandiyan[4], Veluchamy Amutha Barathi[3,5,6], Ramkumar Sabesan[4], Leopold Schmetterer[1-3,5,7-10], Tong Ling[1-3]

[1] *School of Chemical and Biomedical Engineering, Nanyang Technological University, Singapore*

[2] *SERI-NTU Advanced Ocular Engineering (STANCE) Program, Singapore*

[3] *Singapore Eye Research Institute, Singapore National Eye Centre, Singapore*

[4] *Department of Ophthalmology, University of Washington, Seattle, WA 98109, USA*

[5] *Department of Ophthalmology, Yong Loo Lin School of Medicine, National University of Singapore and National University Health System, Singapore*

[6] *Academic Clinical Program in Ophthalmology, Duke-NUS Graduate Medical School, Singapore, Singapore*

[7] *Department of Ophthalmology, Lee Kong Chian School of Medicine, Nanyang Technological University, Singapore*

[8] *Department of Clinical Pharmacology, Medical University of Vienna, Austria*

[9] *Center for Medical Physics and Biomedical Engineering, Medical University of Vienna, Austria*

[10] *Institute of Molecular and Clinical Ophthalmology, Basel, Switzerland*

Corresponding author: Tong Ling (tong.ling@ntu.edu.sg)

Abstract:

Phase-sensitive Fourier-domain optical coherence tomography (FD-OCT) enables label-free imaging of cellular movements in vivo with detection sensitivity down to the nanometer scale. Due to this high sensitivity, it is widely employed in various emerging functional imaging modalities such as optoretinography (ORG), optical coherence elastography (OCE), and optical coherence tomography angiography (OCTA). However, achieving shot-noise limited detection sensitivity remains a major challenge for in-vivo measurements where the sample is constantly affected by vascular pulsation, breathing, eye and head motion, and other involuntary movements. Here, we propose a phase-restoring subpixel motion correction (PRSMC) method for post-hoc image registration in FD-OCT. Based on a generalized FD-OCT model, this method enables translational shifts of OCT images by arbitrary displacements while accurately restoring physically meaningful phase components, both with subpixel precision. With the sample movements estimated from averaged Doppler shift or normalized cross-correlation, we reconstructed the OCT images by correcting the axial displacement in the spectrum (k) domain and the lateral displacement in the spatial frequency domain, respectively. We validated our method in simulations, phantom experiments, and in-vivo optoretinogram imaging, where the advantages over conventional approaches for both amplitude stability and phase accuracy were demonstrated. Our approach significantly reduces the motion-induced phase error (MIPE) when imaging moving samples, achieving systematic phase sensitivities close to the shot-noise regime.

1. Introduction

Fourier-domain optical coherence tomography (FD-OCT) realizes depth-resolved imaging via the Fourier transform of spectral interference between the back-scattered light from the sample and the reference beam [1]. While conventional OCTs utilize the amplitude component of OCT signals that represents the light intensity scattered from anatomical microstructures, phase-sensitive OCT (PhS-OCT) exploits the phase difference between repeated A-scans [2, 3], B-scans [4, 5] or volumetric scans [6] to achieve imaging of structural dynamics with sensitivity down to the nanometer regime [7]. Compared with conventional OCTs, the detection sensitivity of PhS-OCT is not limited by the optical resolution, but rather, scales inversely proportional to the square root of the OCT signal-to-noise ratio (SNR) [8]. Owing to such a high motion sensitivity, PhS-OCT has led to the development of several label-free functional imaging modalities. For instance, Doppler OCT has been widely used in velocimetry to quantify the blood flow velocity [9, 10], while optical coherence elastography (OCE) was developed to evaluate tissue biomechanical properties [11, 12]. Recently, the application of PhS-OCT to image the functional activity of photoreceptors in response to light stimulus, generally termed optoretinography (ORG), has sparked significant interest in scientific research and clinical diagnosis [13-16]. Besides, PhS-OCT may open the door to all-optical interferometric thermometry for non-damaging photothermal therapies [17, 18].

Despite the ever-growing impact of PhS-OCT, previous studies mainly treated the measured phase difference between repeated scans as the sum of the Doppler shift and the SNR-related shot noise. Some studies have delved into the accuracy of phase measurements in moving samples [19-22], and their results suggested the motion as an additional source of phase noise that reduces the correlation of the measured Doppler shift. Besides, when quantifying the flow velocity or the local tissue deformation within a moving sample, such as in Doppler OCT, ORG, and interferometric thermometry, the sample's bulk motion with respect to the OCT imaging system will strongly affect the phase stability [16]. This is especially problematic for in-vivo measurements where the sample is constantly affected by vascular pulsation, breathing, and other involuntary movements. In both scenarios, the motion itself precludes a shot-noise limited motion sensitivity from being achieved.

Fundamentally, the extra phase uncertainty introduced by the translational motion can be seen to result from the variation of each scatterer's weight in contribution to the complex-valued OCT signal at the pixel of interest, which behaves like a deterministic *error* instead of a stochastic *noise* if the scatterers' relative locations remain fixed in the sample [23]. More specifically, the complex-valued OCT signal at each sampling pixel is a weighted superposition of coherent light signals scattered from adjacent scatterers confined by the coherence gating, and their weights are determined by the point spread function (PSF) centered at that pixel [24, 25]. Thus, when measuring the sample movement using the phase signals in Doppler OCT or OCE, the movements will instantaneously change the PSF vs. pixel relationship in space and inevitably alter the weights of the scattering signal superposition, leading to the extra phase error, termed motion-induced phase error (MIPE) in this article. Nevertheless, if we can accurately restore identical sampling pixels throughout the sample movement, it is also possible to eliminate the MIPE. One practical solution is to use post-hoc image registration algorithms to shift the OCT images back to the initial sampling pixels, which can be generally achieved through motion estimation and image correction.

The post-hoc OCT image registration can be implemented at different scales, including among: a) individual A-lines with a single degree of freedom (DoF) (z) in the depth direction, b) individual B-scans

with 2 DoFs (x, z) for repeated cross-sectional scans, and c) individual B-scans with 3 DoFs (x, y, z) for repeated volumetric scans. For image registration with only 1 DoF in the z-direction, the axial displacements between adjacent A-lines were typically estimated with histogram-based normalization [4, 20] or averaged phase difference [26, 27], while motion correction was conducted by subtracting the estimated Doppler shift introduced by bulk motion [4, 20] or multiplying a complex-valued exponential term in the spectrum (k) domain [26, 27]. Although both correction approaches were able to retrieve physically meaningful phase components, none of the previous studies have systematically analyzed the MIPE. For high-speed phase-sensitive OCT imaging with repeated cross-sectional B-scans or repeated volumetric C-scans, image registration must be conducted in 2 or 3 DoFs in both the axial and the lateral directions. In previous studies, translational displacements between the reference and target images were estimated using normalized cross-correlation (NCC) based [28-31] or phase-only correlation (POC) based methods [32], while the image correction was achieved by shifting the complex-valued target image [33-35] or the 2~4 fold upsampled target image [28, 29] in the unit of pixels. However, these techniques can only shift the OCT image by discrete distances restricted by the upsampling rate, and the computational and storage load will increase dramatically with more refined displacements. To correct arbitrary displacements, another method is to directly multiply the Fourier transform (FT) of the target image by a complex-valued exponential term, termed FT-based correction in this article [28, 30]. But the FT-based correction method simply treats the OCT images as conventional digital images and corrects both the axial and lateral displacements in the spatial frequency domain. When the axial sampling rate is limited, it cannot accurately restore the complex-valued OCT signals and will introduce severe side lopes unexpectedly.

In this article, we propose a phase-restoring subpixel motion correction (PRSMC) approach to eliminate the MIPE in FD-OCT. Starting from a general FD-OCT model, we derived the root causes of phase inaccuracy when imaging moving samples, which laid the theoretical foundation for our subpixel image reconstruction method. Besides, we analyzed the influence of the MIPE on localization accuracy in numerical simulations, which was further validated in synthetic phantom experiments. We also compared the phase accuracies using conventional and PRSMC registration methods when detecting nanoscopic deformation in moving samples. Moreover, with phantom experiments and in-vivo ORG imaging in humans and wild-type rats, we demonstrated that the phase instabilities in these measurements can be reduced to a large extent using our PRSMC method, leading to systematic detection sensitivities close to shot-noise limit.

2. Methods

2.1 Translational motion model and the origin of motion-induced phase error

Compared with rotational motion, translational motion is the dominant source of motion artifact in high-speed OCT imaging, hence we only consider and correct translational shifts between the reference image and the target image in this study. Assuming that the measured sample was shifted by Δx and Δz pixels in the lateral (x) and the axial (z) directions, where Δx and Δz can be decimals, the complex-valued OCT signals $\widetilde{A_R}$ and $\widetilde{A_T}$ of the reference and target images should satisfy the following relation:

$$\widetilde{A_T}(x, z) = \widetilde{A_R}(x - \Delta x, z - \Delta z) \cdot \exp(i2k_0\delta z), \tag{1}$$

where k_0 denotes the center wavenumber of the light source. The exponential term $\exp(i2k_0\delta z)$ represents the phase change induced by the change of optical path length (OPL), where δz is the physical displacement equal to Δz multiplied by the axial pixel size.

Although it is well known that the transverse motion itself will reduce the correlation between consecutively measured OCT signals [16, 20-22], the effect of axial bulk motion was neglected in most previous studies [19]. To further investigate the origins of the MIPE, we modeled the OCT signal of each pixel as the convolution of a PSF with surrounding scatterers. Given a laser beam with a Gaussian profile and a Gaussian-shaped spectrum of the light source, the PSF $h(x,z)$ of the OCT system can be described as [19, 24, 25],

$$h(x,z) = \exp\left(-2\frac{x^2}{w_l^2}\right)\exp\left(-2\frac{z^2}{w_z^2}\right)\exp(2ik_0 z), \tag{2}$$

where w_l is the $1/\mathrm{e}^2$ spot diameter of the OCT beam focused on the sample, and w_z is the $1/\mathrm{e}^2$ width of the axial PSF.

Assuming that a set of scatterers are arbitrarily distributed around the pixel of interest and then shifted by physical displacements δx and δz in the lateral and axial directions, the object intensities of the scatterers in the reference frame $\eta_R(x,z)$ and target frame $\eta_T(x,z)$ can be modeled as,

$$\eta_R(x,z) = \sum_j R_j \delta\left(x - x_j, z - z_j\right), \tag{3}$$

$$\eta_T(x,z) = \sum_j R_j \delta\left(x - x_j - \delta x, z - z_j - \delta z\right), \tag{4}$$

where $\delta(\,)$ is the Dirac delta function, j is the index of scatterers, R_j and $\left(\mathrm{x}_j, z_j\right)$ denote the reflectivity and the coordinate of the jth scatterer.

The OCT signals $\widetilde{A_R}$ and $\widetilde{A_T}$ measured from the same pixel in the reference and target frames will be,

$$\widetilde{A_R} = h(x,z)\otimes\eta_R(x,z) = \sum_j R_j \exp\left(-2\frac{x_j^2}{w_l^2}\right)\exp\left(-2\frac{z_j^2}{w_z^2}\right)\exp\left(2ik_0 z_j\right) = \sum_j R_{Rj}\exp\left(2ik_0 z_j\right), \tag{5}$$

$$\begin{aligned}\widetilde{A_T} = h(x,z)\otimes\eta_T(x,z) &= \sum_j R_j \exp\left[-2\frac{(x_j+\delta x)^2}{w_l^2}\right]\exp\left[-2\frac{(z_j+\delta z)^2}{w_z^2}\right]\exp\left[2ik_0\left(z_j+\delta z\right)\right] \\ &= \exp(2ik_0\delta z)\cdot\sum_j R_{Tj}\exp\left(2ik_0 z_j\right),\end{aligned} \tag{6}$$

where $\otimes$ denotes the convolution operation, $R_{Rj} = R_j \exp\left(-2\frac{\mathrm{x}_j^2}{w_l^2}\right)\exp\left(-2\frac{z_j^2}{w_z^2}\right)$ and $R_{Tj} = R_j \exp\left[-2\frac{(\mathrm{x}_j+\delta\mathrm{x})^2}{w_\mathrm{l}^2}\right]\exp\left[-2\frac{(z_j+\delta z)^2}{w_z^2}\right]$ are defined as the PSF weighted reflectivity for scatterers in the reference and target frames.

Therefore, the phase difference $\Delta\varphi$ between the measurements $\widetilde{A_R}$ and $\widetilde{A_T}$ can be written as,

$$\Delta\varphi = \arg\left(\widetilde{A_R}^*\widetilde{A_T}\right) = 2k_0\delta z + \arg\left(\sum_j R_{Rj}\exp\left(-2ik_0 z_j\right)\cdot\sum_j R_{Tj}\exp\left(2ik_0 z_j\right)\right), \tag{7}$$

where $\arg(\,)$ denotes the calculation of argument, and $\widetilde{A_R}^*$ is the conjugate of $\widetilde{A_R}$.

Eq. (7) shows that in addition to an expected Doppler phase shift $2k_0\delta z$, the phase difference will also be affected by an extra error term due to the difference in the PSF weighted reflectivity. Here, we term such an error as motion-induced phase error or MIPE.

2.2 Phase-restoring subpixel motion correction (PRSMC) of FD-OCT images

According to the general FD-OCT model (see Supplementary Section 1), the complex-valued spectral signals of the reference frame and the target frame with a translational shift of $(\Delta x, \Delta z)$ pixels should satisfy the following relation [26, 27],

$$\widetilde{I_R}(x-\Delta x, k_{Sn}) = \widetilde{I_T}(x, k_{Sn}) \circ \exp(-i2k_{Sn}\delta z)$$
$$= \widetilde{I_T}(x, k_{Sn}) \cdot \exp(-i2k_0\delta z) \circ \exp[-i2(k_{Sn}-k_0)\delta z], \quad (8)$$

where $\widetilde{I_R}$ and $\widetilde{I_T}$ are the complex-valued spectral signals of the reference frame and the target frame, $\circ$ denotes Hadamard product, and k_{Sn} represents discrete sampling points in the k domain.

More specifically, the first exponential term $\exp(-i2k_0\delta z)$ accounts for the Doppler shift due to the change of OPL, and the second pixel-wise exponential term $\exp[-i2(k_{Sn}-k_0)\delta z]$ corresponds to the extra error introduced by the axial bulk motion. Therefore, in practice, correcting the axial motion by multiplying both terms enables accurate reconstruction of complex-valued OCT images as if the sample was physically shifted back, as written in Eq. (9),

$$\widetilde{I_c}(x, k_{Sn}) = \widetilde{I_T}(x, k_{Sn}) \cdot \exp(-i2k_0\delta z) \circ \exp[-i2(k_{Sn}-k_0)\delta z], \quad (9)$$

where $\widetilde{I_c}$ is the accurately reconstructed complex-valued spectral signal after the axial correction.

Alternatively, image correction by multiplying only the second term will eliminate the extra MIPE while retaining the Doppler shift, which is useful when the Doppler shift is of interest, as shown in Eq. (10),

$$\widetilde{I_c}'(x, k_{Sn}) = \widetilde{I_T}(x, k_{Sn}) \circ \exp[-i2(k_{Sn}-k_0)\delta z], \quad (10)$$

where $\widetilde{I_c}'$ is the complex-valued spectral signal with the MIPE corrected and the Doppler shift retained after the axial correction.

In terms of the lateral direction, given that the Nyquist sampling rate can be satisfied, we can correct the transverse subpixel motion in the spatial frequency domain, which can be written as [28, 36, 37]:

$$\mathcal{F}\{\widetilde{A_C}(x,z)\} = \mathcal{F}\{\widetilde{A_T}(x,z)\} \circ \exp\left(i\frac{2m_x\pi}{M_x}\Delta x\right), \quad (11)$$

where $\widetilde{A_C}$ is the reconstructed complex-valued OCT signal after lateral correction, m_x ranges from $-(M_x-1)/2$ to $(M_x-1)/2$ and M_x denotes the total number of pixels in the lateral x direction.

The procedures of our proposed PRSMC method are illustrated in Fig. 1. To correct the axial displacement, the complex-valued spectral signal $\tilde{I}(k_{Sn})$ can be obtained by numerical Hilbert transform: $\tilde{I}(k_{Sn}) = I(k_{Sn}) + iH\big(I(k_{Sn})\big)$, where $I(k_{Sn})$ is the recorded real-valued spectral signal on the detector [26]. A phase map determined by Eq. (9) or Eq. (10) will be applied to shift the phase component of the spectral signal. The axially shifted images will then be reconstructed by conducting discrete Fourier transform (DFT) of the shifted spectral signal along the k direction and removing the negative frequency part. In comparison, to correct the lateral displacement, the OCT image will at first be transformed into the spatial frequency (u) domain by performing DFT along the x direction. The spatial frequency signal will then be multiplied with the phase map determined by Eq. (11). Eventually, the laterally shifted OCT image can be reconstructed by transforming the spatial frequency signal back to the spatial domain with inverse discrete Fourier transform (iDFT) along the u direction. In contrast, previous FT-based method treated the OCT images as conventional digital images and corrected both

the axial and lateral displacements in the spatial frequency domain in the same manner (see Supplementary Section 2).

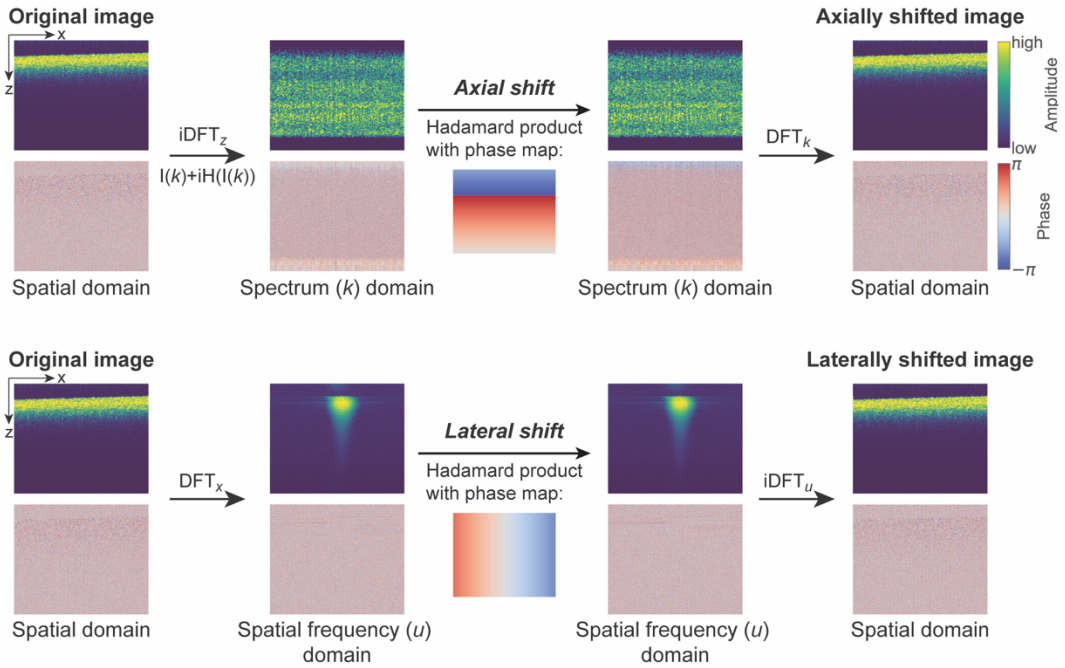

Fig. 1. Schematic diagram of the proposed PRSMC method. To correct the axial displacement, the complex-valued spectral signal obtained by numerical Hilbert transform will be multiplied by the phase map determined by Eq. (9) or Eq. (10). Then the axially shifted image can be reconstructed by the DFT of the shifted spectral signal. As for correcting the lateral displacement, the spatial frequency domain signal obtained by the DFT of the complex-valued OCT image along the x direction will be multiplied by a phase map determined by Eq. (11). The laterally shifted OCT image can be reconstructed by taking the iDFT along the lateral spatial frequency direction.

2.3 Subpixel motion estimation for repeated cross-sectional scans and repeated volumetric scans

In the phantom experiment, the subpixel-level axial bulk motion was estimated by the averaged Doppler phase shift extracted from the phantom surface. For rodent optoretinogram (ORG) experiment, we adopted the single-step DFT approach [30, 31] to estimate the subpixel-level displacements between repeated cross-sectional B-scans. In brief, a 2-fold upsampled NCC function was first obtained by zero-padding in its Fourier domain and the location of its peak was found as the initial estimation. Since only a small neighborhood around the NCC peak is of interest, the matrix-multiply DFT method was used to compute the κ-fold upsampled NCC map in a 1.5×1.5 pixel neighborhood centered on the initial estimation. In this study, κ was set to 1000 to allow motion estimation with sufficiently small intervals. Compared with conventional upsampling strategy using fast Fourier transform (FFT), the matrix multiplication approach greatly reduces the computational load.

For repeated volumetric C-scans in human ORG experiment, we followed the coarse-to-fine strategy proposed by Do et al. to estimate the translational motion of individual B-scans [34, 35], except that in the fine estimation step, we adopted single-step DFT approach to extend the previous pixel-level estimation to subpixel-level in the depth (z) and the fast-scan (x) dimensions. Briefly, in the coarse

estimation step, a set of target sub-volumes consisting of several consecutive B-scans were selected from the target volume, and their positions in the reference volume were estimated with three-dimensional (3D) NCC method. Then, by linearly interpolating the obtained sparse coarse shifts, the coarse shift in the slow-scan (y) direction for each B-scan can be computed. In the fine estimation step, for each target B-scan, a reference sub-volume was defined according to its coarse shift in the y direction. The single-step DFT method was used to calculate the correlation between each target B-scan and individual B-scans in its corresponding reference sub-volume. Finally, the coordinate with the maximum correlation value was found as the estimated displacement for each target B-scan.

2.4 Numerical simulation

All numerical simulation experiments were conducted based on a close-to-reality model for simulating speckle-pattern evolution in FD-OCT [38]. In this model, a predefined number of scatterers with equal reflectivity were generated and assigned to uniformly distributed random coordinates. The average density of the scatterers was set to be 5 per coherence length to obtain fully developed speckle pattern [19, 38]. Then the interference spectrum signal in each A-line was calculated based on Eq. (S1) (see Supplementary Section 1) and transformed into the OCT image in spatial domain by DFT. The simulation parameters, including the central wavelength and the bandwidth of the light source, as well as the sampling points on the calibrated k domain, were set to be consistent with our point-scan OCT system used in this study. Both the power spectrum $S(k_{sn})$ of the light source and the laser beam profile were modelled with a Gaussian function. The interval between adjacent A-scans was set to be half the full-width-at-half-maximum (FWHM) of the lateral PSF. Translational motion of the sample was achieved by changing the coordinates of all the scatterers in the forward FD-OCT model numerically.

2.5 Point-scan OCT system

A custom-built spectral-domain point-scan OCT system, as described in previous study was employed for both phantom and rodent optoretinogram (ORG) experiments [39]. In brief, this system uses a superluminescent diode (cBLMD-T-850-HP-I, Superlum, Ireland) with a central wavelength of 850 nm and a FWHM bandwidth of 165 nm, providing a theoretical axial resolution of 1.9 $\mu\mathrm{m}$ in air. The detector of this OCT system is a spectrometer equipped with a line-scan camera (OctoPlus, Teledyne e2v, UK) with a maximum acquisition rate of 250,000 lines per second for 2048 pixels, which allows an imaging depth of 1.07 mm in air. The sample arm can be modified according to specific imaging requirements. For phantom experiments, an objective lens was placed after the galvo scanner to focus the beam on the sample and achieved a lateral resolution of 3.3 $\mu\mathrm{m}$ in air. For rodent ORG experiment, a scan lens (80 mm doublet) and an ocular lens (30 mm and 25 mm doublet) were used to conjugate the galvo scanner to the pupil plane. Their focal lengths were chosen to achieve smaller beam size and enlarged field of view. The theoretical lateral resolution was estimated to be 7.2 $\mu\mathrm{m}$ based on a standard rat eye model [40].

2.6 Phantom fabrication and imaging protocol

A synthetic phantom was fabricated by mixing TiO_2 powder and Polydimethylsiloxane (PDMS) with a weight ratio of 5%. The mixture was then vacuumed for 20 minutes and cured in an oven (90 °C) for 30

minutes. A phantom patch ($2 \times 2 \times 1$ mm) was cut off and attached to the surface of a high-precision piezo actuator (P-888.91, Physik Instrumente, Germany). A cover glass, as a static reference, was glued to a lens mount and placed over the phantom without contact. The base of the piezo actuator and the cover glass were connected to the last lens of the OCT sample arm using mechanical frames to reduce the disturbance from environmental vibration. The piezo actuator was driven by a sinusoidal voltage with a frequency of 1 Hz, resulting in controlled vibration at the same frequency in the axial direction. In the recording, a total of 600 repeated B-scans were acquired at the same position, while each B-scan, consisting of 1000 A-lines, takes 5 ms.

2.7 Animal preparation and optoretinogram imaging

The experiments were conducted in accordance with the guidelines and approval from Institutional Animal Care and Use Committee (IACUC), SingHealth (2020/SHS/1574). Brown Norway rats were anesthetized with ketamine and xylazine cocktail. The animals were fixed in a custom-built stereotaxical holder with integrated bite bar and ear bar to mitigate the eye movements induced by breathing and heartbeat. Before the OCT imaging, the pupil of the animal was dilated with a drop of 1% Tropicamide (Alcon, Geneva, Switzerland) and 2.5% Phenylephrine (Alcon, Geneva, Switzerland). During the imaging, the cornea was kept moist with a balanced salt solution.

To measure the rodent ORG in vivo, visual stimulation was generated by a white light LED (MBB1L3, Thorlabs, USA). The beam was collimated by an aspheric condenser lens and filtered by a narrow bandpass filter (500±5 nm, #65-694, Edmund Optics, Singapore). Then, the stimulation light was converged by the ocular lens (30 mm and 25 mm doublet), resulting in a 43.4° Maxwellian illumination on the posterior eye. In each recording, 800 repeated B-scans were acquired at the same position with each B-scan consisting of 1000 A-lines. Each dataset took a total acquisition time of 4 seconds, while a short flash with a duration of 1 ms was delivered to the eye 1 second after the recording started.

The phase difference between the inner segment/outer segment junction (IS/OS) and the rod outer segment (ROS) was extracted for evaluating the functional response of photoreceptors to light stimulus. The IS/OS and ROS were segmented using an automatic segmentation algorithm based on graph theory and dynamic programming [41]. In addition, to exclude the disturbance from superficial large vessels, a binary OCT angiogram was generated by setting an adaptive threshold on the inverse SNR and complex-valued decorrelation space [42].

2.8 Adaptive optics line-scan OCT system for human optoretinogram imaging

A custom-built adaptive optics (AO) line-scan OCT system was constructed for human ORG imaging [13, 16]. In brief, the line-scan SD-OCT channel uses a supercontinuum light source (SuperK EXR-9OCT, NKT Photonics, A/S, Birkerød, Denmark) centered at 820 nm with a FWHM bandwidth of 80 nm, providing a theoretical axial resolution of 4.3 μm in air. A cylindrical lens (ACY254-75-B, Thorlabs Inc.) and a 1D galvo-scanner (6210H, Cambridge Technology, USA) were used to achieve a $1.3° \times 1°$ field of view on retina. The detector of the OCT system is a spectrometer consisting of a diffraction grating with 600 line pairs per millimeter and a high-speed 2D camera (Photron, FASTCAM Mini Ax200). The camera was configured with a resolution of 896 (spectrum dimension) × 512 (line dimension) pixels, allowing an axial imaging range of 2.0 mm and a maximum frame rate of 16.2 kHz. The AO subsystem uses a 980±10

nm superluminescent diode (IPSDD0906, Inphenix, USA). A custom-made Shack-Hartmann wavefront sensor and a deformable mirror (ALPAO, DM97-15, France) were incorporated to measure and correct ocular aberrations.

For human optoretinogram imaging, the experiment was approved by the University of Washington Institutional Review Board and was conducted in compliance with the tenets of the Declaration of Helsinki. All subjects signed an informed consent before their participation. Subjects without retinal disease were enrolled in the study. Before the OCT imaging, cycloplegia was introduced with Tropicamide 1% ophthalmic solution (Akorn Inc.) to dilate the pupil and increase numerical aperture. To record the human ORG signal, the subject was dark adapted for 3 to 4 minutes. In each recording, 40 volumes were acquired at a volume rate of 15 Hz with each volume consisting of 400 B-scans. The 20-ms visual stimulation was generated by a 660$\pm$10 nm LED in Maxwellian view onto the retina after 10 volumetric scans.

3. Results

3.1 Numerical validation of MIPE and its accurate correction by PRSMC

To validate the MIPE, we conducted numerical simulations based on a close-to-reality model that can simulate speckle patterns in FD-OCT (see Methods). As shown in Fig. 2, we gradually translated the simulated sample in the axial direction by 3 μm with a step of 0.01 μm. The phase differences between those of the subsequent positions and that of the initial position were calculated and unwrapped to obtain the phase change of each pixel (Fig. 2a). Instead of seeing the phase changes in all pixels being consistent with the global translational shifts, we observed an error band of phase changes around a peak that corresponds to the actual displacement of the simulated sample, which fits the prediction of our theoretical analysis (see Methods). Moreover, as the OCT image gradually decorrelated when the displacement increased to 3 μm, the error band of the phase changes also increased dramatically.

Intriguingly, our PRSMC method can restore the translationally shifted OCT image back to its original position as if the sample was maintained at the same location physically, thus eliminating the difference in the PSF weighted reflectivity in Eq. (7). As shown in Figs. 2b and 2c, the phase error resulting from the sample motion was eliminated in our simulation results. As plotted in Fig. 2c, for the raw phase signal without correction, the STD of the displacement extracted from the raw phase was ~1.1 nm when the sample was moved by 10 nm, and this value gradually increased to ~150 nm when the motion increased to 3 μm. In comparison, the STD of the corrected phase signals kept at almost zero, where the remaining deviations were likely due to the numerical errors in those pixels with extremely low signal intensity. Further analysis compared with the FT-based method confirms the advantage of our approach in correcting subpixel-level displacement, whereas the FT-based method even degrades the signal stability (Supplementary Section 3).

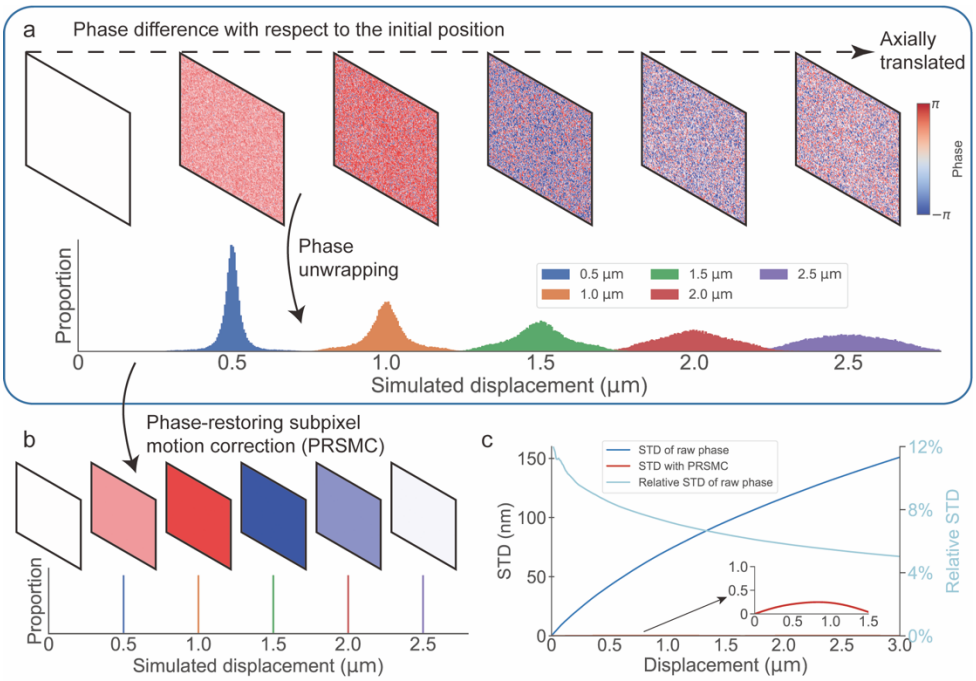

Fig. 2. Simulation analysis of the phase measurement accuracy obtained from the raw phase signal and the phase signal corrected by PRSMC. (a) Top: Differences between the phase signal acquired at subsequent positions with respect to that at the initial position. Bottom: The distribution of the displacements extracted from the phase differences after phase unwrapping along the time dimension. (b) The phase differences and the distribution of displacement obtained after PRSMC. (c) The blue and red curves show the STDs of the displacements obtained by the raw phase and the corrected phase as a function of the actual sample displacement. The cyan curve shows the ratio between the STD of the displacement obtained from the raw phase signal and the actual displacement.

3.2 Shot-noise limited phase sensitivity achieved in imaging moving phantom

Phantom experiments were conducted to further demonstrate the validity of our PRSMC method in correcting the MIPE. As shown in Fig. 3a, a synthetic phantom made of TiO_2 and PDMS (see Methods) was fixed on a piezo actuator that was driven by a sinusoidal voltage, and we used a cover glass serving as a static reference to cancel the phase drift of the OCT system. Due to the MIPE, apparent deviations were observed in the motion measured by the phase of phantom surface (as shown by the blue curves in Fig. 3b). An average of these curves was calculated as the estimated sample displacement for subsequent image correction. As illustrated by the red curves in Fig. 3b, the motion dependent error was greatly suppressed after the PRSMC, leading to consistent motion measurements across all pixels. The motion detection accuracy from the phase signal of speckles was also measured. As shown in Fig. 3c, after correction with PRSMC approach and removing outliers (see Supplementary Section 4), the variation in the measured motions was significantly reduced. To quantitatively evaluate the phase error, the mean value of each method (Fig. 3d) was subtracted from the phase signals at individual pixels to exclude the influence of the Doppler shift (Fig. 3e). Then the STDs of residual phase in time were calculated for each individual pixel and compared with the theoretically estimated shot noise [8]. As illustrated in Fig. 3f, for the phase extracted from the surface, the phase error after PRSMC (55.6±23.4 mrad, mean±STD) was close to the theoretical shot noise level (46.7±19.3 mrad), and was

significantly lower than that of the raw phase without correction (480.1±190.0 mrad). For the phase extracted from the speckles, the phase stability was significantly improved from 758.0±381.6 mrad to 87.4±23.6 mrad after PRSMC, compared with a theoretical shot noise of 72.8±22.2 mrad. The remaining difference from the shot noise level may be due to the out-of-plane motion that we were unable to correct in the repeated B-scan mode.

Figure 3g shows the distribution of the motion measured from the phase of speckles at 5 different time points (as labelled in Fig. 3c). Compared with the distribution extracted from the raw phase (the bottom gray areas), the PRSMC method (the colored areas) significantly suppressed the phase error and achieved a much sharper measurement distribution. As shown in Fig. 3h, the STDs of the measurement distribution obtained by each configuration was calculated at each time point. With the increasing of the axial displacement, the uncertainty of phase measurement gradually increased, whereas a uniform measurement uncertainty was obtained after PRSMC. As shown in Fig. 3i, the corrected phase greatly reduces the MIPE and achieves measurement accuracy comparable to that limited by shot noise (compare the red and pink lines with the dashed black line).

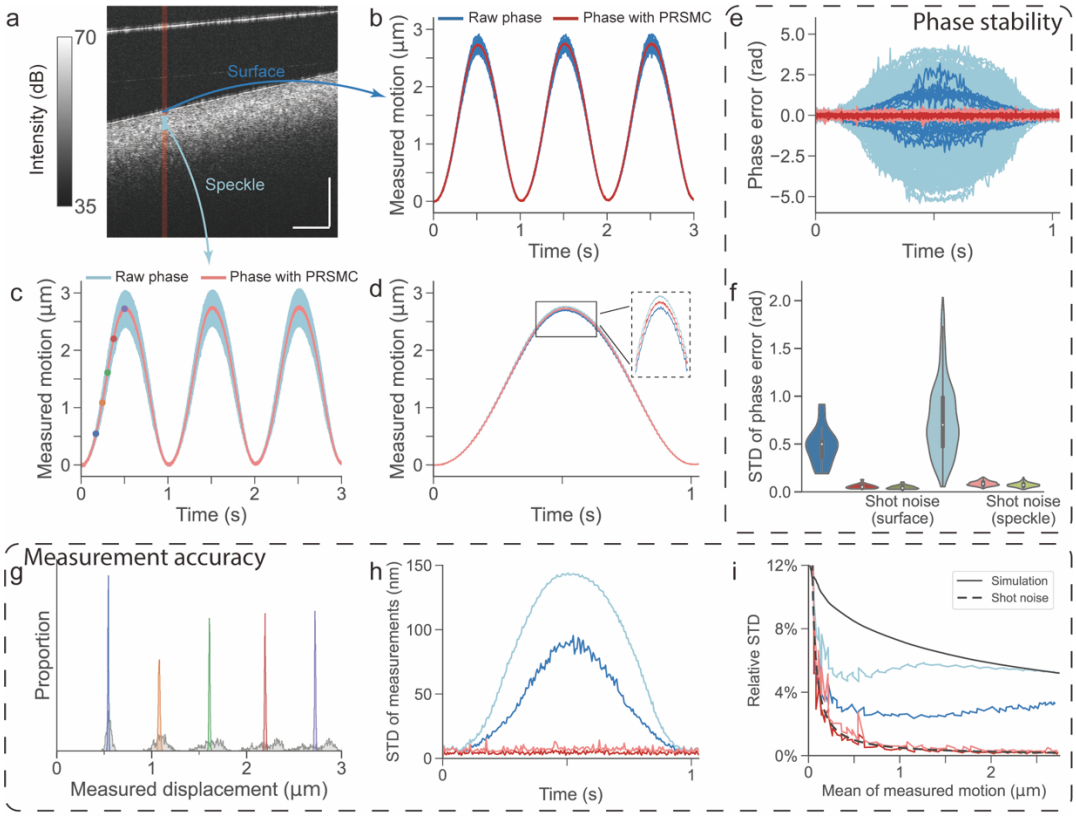

Fig. 3. Phantom experiment was conducted to validate the MIPE derived from theoretical analysis and our proposed PRSMC method. (a) A structural OCT image of the phantom's cross-section. Scale bar: 300 μm. (b) The motion measured from the phase on the phantom surface without (blue curves) and with (red curves) correction in 20 adjacent A-lines (the blue region in Fig. 3a). (c) The motion measured from the phase of the speckles inside the phantom (the cyan region in Fig. 3a) without (cyan curves) and with correction (pink curves). (d) Average curves of all phase signals measured at individual pixels in four configurations (on the surface or from the speckles & without or with correction), each comes with a curve corresponds to the legends in (b) and (c). Inset is the enlarged view of the curves enclosed by the black rectangle. (e) The residual phase signals at individual pixels calculated by subtracting the average curve obtained using the same configuration. (f) The STDs of residual phases under different configurations and the theoretically estimated shot noise of the surface and interior of the phantom. (g) Distribution of the

motion measured from the speckle phase at 5 time points (as labeled in Fig. 3c). The bottom gray distributions denote the motion measured from the raw phase, while the colored distributions correspond to the measured motion after PRSMC. (h) The STDs of all the phase signals measured from individual pixels at each time point in all four configurations. (i) The ratio of the measurement STDs to the mean of measured motion. In addition to colored lines corresponding to the four configurations, the solid and dashed black lines represent the measurement accuracy obtained from the simulation analysis and that limited by the shot noise.

3.3 Significantly improved amplitude stability and phase accuracy when detecting nanoscopic motion within moving samples

In this section, numerical simulations and ORG experiments were conducted to reveal the influence of bulk motion on measuring nanoscopic motion within sample. The subpixel bulk motion, if remains uncorrected, will introduce unexpected phase error and reduce the accuracy of measured nanoscopic OPL change. Our results show that the PRSMC method can effectively reconstruct the structural image while suppressing the MIPE, improving the accuracy of the phase measurement.

In numerical simulation, we modeled a sample with two layers, each consisting of 5 pixels. We first translated the bottom layer axially by 50 nm, and then the entire sample was gradually shifted in the axial direction up to 2.5 pixel with a step of 0.01 pixel (see Supplementary Section 5). The phase difference between the center pixels in both layers was calculated to evaluate the deformation between these layers. As shown in Fig. 4a, after conventional pixel-level correction (Fig 4a, top), the residual subpixel-level motion still broadens the simulated phase difference, degrading the accuracy in detecting the sample deformation. In comparison, the PRSMC method (Fig. 4a, bottom) can dramatically reduce the error band resulting from the bulk motion, while the remaining error was introduced by the deformation process. Figure 4b shows the STDs of the phase signals obtained using different correction methods, which clearly demonstrates the superiority of the PRSMC method over pixel-level correction methods on suppressing the MIPE.

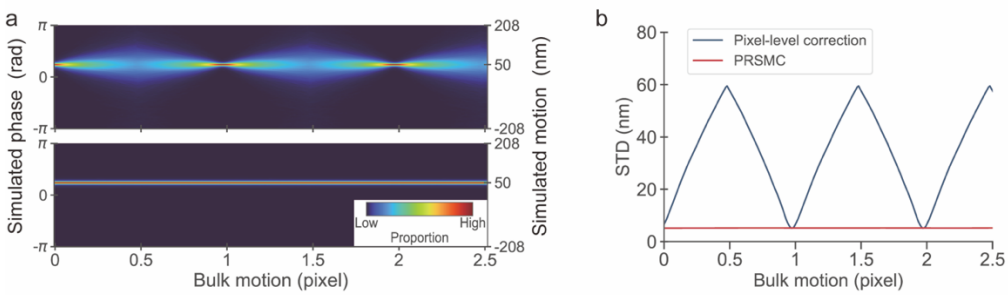

Fig. 4. Simulation analysis of the influence of residual bulk motion on detecting the nanoscopic deformation within a moving sample. (a) The distribution of the simulated phase at all pixels of interest after pixel-level image correction (top) or PRSMC method (bottom). (b) STDs of the deformation obtained after correction using different methods.

To investigate whether our PRSMC method can be applied to improve in-vivo retinal imaging, we conducted optoretinogram imaging in human and rat retinas. In the first protocol, we conducted repeated B-scans in a wild-type rat's retina using a point-scan OCT system. Fig. 5a shows the structural image and the time-elapsed M-scan consisting of repeated A-scans at the same location. As shown in Fig. 5b, we estimated the bulk motion of the retina using the efficient single-step DFT approach (see

Methods). The apparent bulk motion in the original uncorrected M-scan (Fig. 5c, top left) can be corrected by our PRSMC method, leaving almost static retinal layers in the M-scan (Fig. 5c, bottom right). In comparison, serrated residual motion remained after pixel-level correction (Fig. 5c, top right), whereas severe side lopes were unexpectedly introduced by FT-based correction (Fig. 5c, bottom left).

In terms of phase stability, the phase difference between the brightest pixels in the inner segment/outer segment junction (IS/OS, the pink area in Fig. 5a) and the rod outer segment (ROS, the cyan area in Fig. 5a) at one A-line was extracted in Fig. 5d. Across the entire field of view, except for the region below large superficial vessels, the STDs of such phase differences in time were reduced to 311.3 ± 105.6 mrad (mean $\pm$ STD) by PRSMC, compared with 351.5 ± 108.9 mrad after pixel-level correction and 343.1 ± 118.9 mrad after FT-based correction. As shown in Fig. 5e, our PRSMC method significantly improved the phase stability compared with the pixel-level correction method. In the ORG measurements using a 1-ms short light stimulus delivered at the time $t = 0$, the PRSMC method results in more stable/less noisy ORG signals compared with the pixel-level correction method (see Fig. 5f). As shown in Fig. 5g, after correction by the PRSMC method, the rodent ORG signal indicating both the early contraction and the late elongation of photoreceptors can be clearly observed.

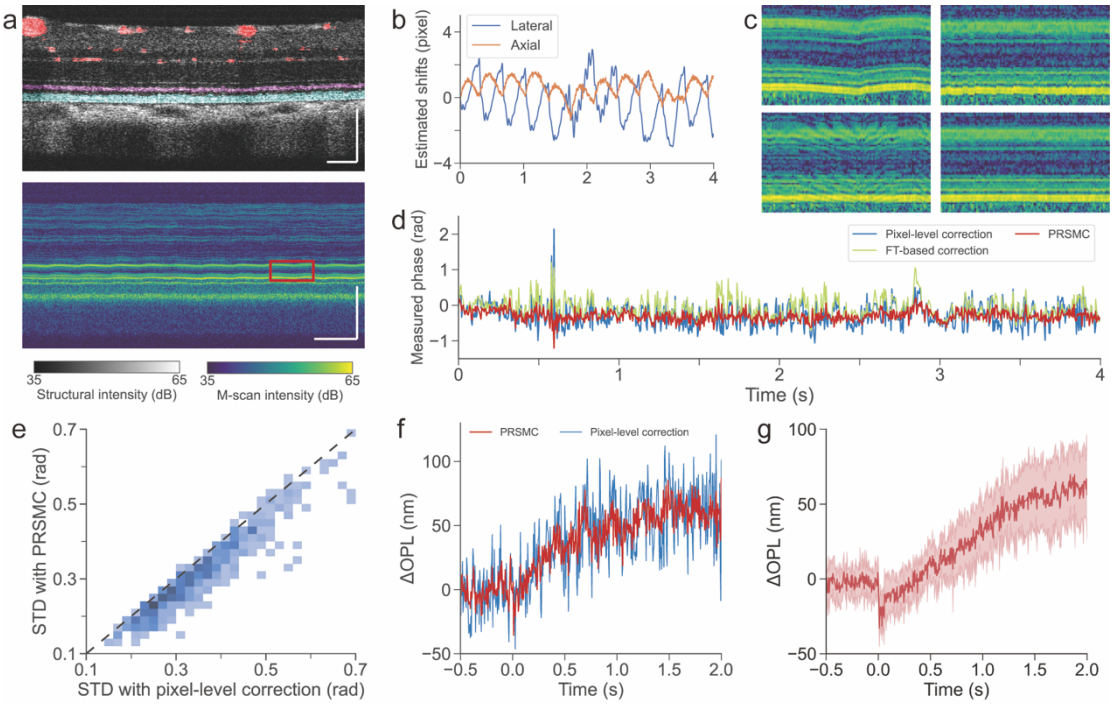

Fig. 5. In-vivo rodent optoretinogram imaging experiment using a non-AO point-scan OCT. (a) Top: structural image of a Brown Norway rat's retina. The pink, cyan, and red areas label the inner segment/out segment junction (IS/OS), the rod outer segment (ROS) and blood vessels, respectively (see Methods). Bottom: a representative time-elapsed M-scan at one A-line. Scale bar in spatial dimension: 200 μm. Scale bar in temporal dimension: 0.5 s. (b) Bulk motion of the retinal tissue estimated by the efficient single-step DFT approach. (c) The enlarged M-scans without correction (top left), and after correction with pixel-level method (top right), FT-based method (bottom left) and the PRSMC method (bottom right). (d) The phase differences between the brightest pixel in IS/OS and ROS on one representative A-line after pixel-level correction (blue line), FT-based correction (green line), and PRSMC (red line), when no light stimulus was delivered to the retina. (e) Distribution of the STDs of the phase fluctuation in different A-lines after pixel-level correction against those after PRSMC. The dashed black line represents the barrier where the two methods yield the same performance. (f) Representative ORG signals after pixel-level correction (blue line) and PRSMC (red

line) obtained from one A-line without averaging. (g) ORG signal of a wild-type rat after PRSMC correction. The red line represents the average of the phase signals at 8 individual locations with high SNR, and the color band denotes the range of their STD.

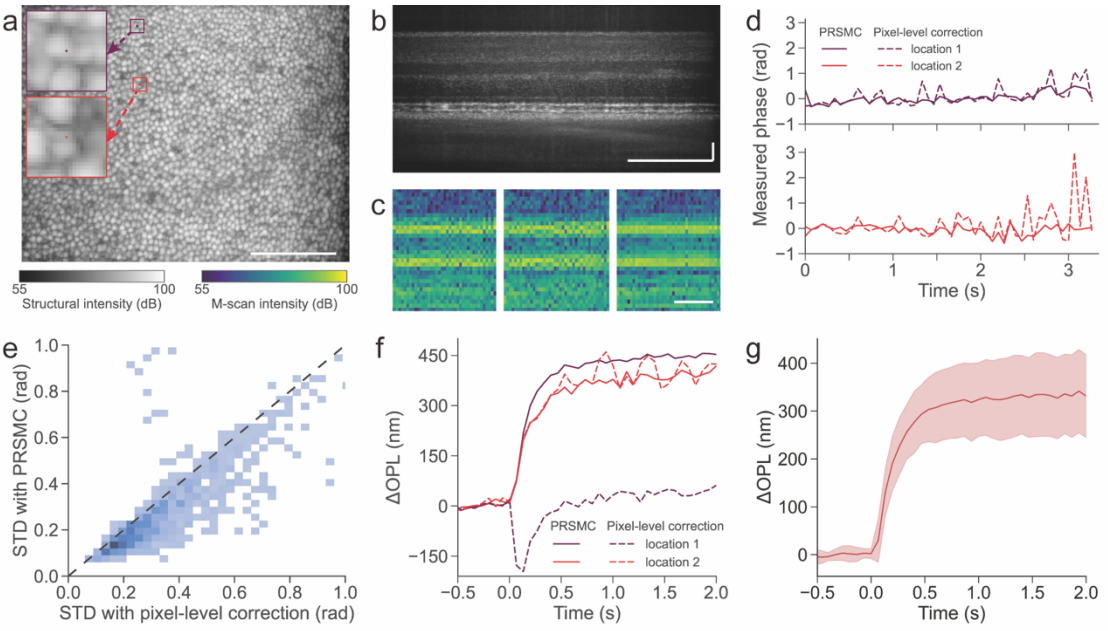

Fig. 6. In-vivo human optoretinogram experiment using an AO line-scan OCT. (a) *En face* image of the cone outer segment tips (COST) layer in a human retina. (b) Cross-sectional structural image of the same retina. Scale bar: 100 μm. (c) Representative time-elapsed M-scans corrected by the pixel-level method (left), FT-based method (middle) and the PRSMC method (right). Scale bar: 1 s. (d) Representative phase differences between the IS/OS and COST at individual A-lines (see Supplementary Section 6) after pixel-level correction (dashed lines), and PRSMC (solid lines), when no light stimulus was delivered to the retina. (e) Distribution of the STDs of the phase differences between the IS/OS and COST boundaries of individual A-lines after pixel-level correction against those after PRSMC. The dashed black line represents the barrier where the two methods yield the same performance. (f) Representative human ORG signals measured from individual A-lines (labeled by the dots in Fig. 6a) showing higher phase stability after PRSMC (solid lines) than those corrected by pixel-level correction (dash lines). (g) Human ORG signal after PRSMC correction. The red line represents the average of the phase signals at 20 individual locations with high SNR, and the color band denotes the range of their STD.

We further tested our proposed method for correcting the bulk motion in repeated volumetric scans of human ORG imaging acquired from a high-speed adaptive-optics line-scan OCT system. Figure 6a and 6b show the *en face* image at the cone outer segment tips (COST) and a structural image at one cross section of the retina. The translational bulk motion of each volume was estimated using the modified coarse-to-fine approach (see Methods). Regarding motion correction performance, our PRSMC method achieves more stable retinal layers (Fig. 6c, right) than the pixel-level correction result (Fig. 6c, left) and the FT-based method (Fig. 6c, middle). Fig. 6d shows the representative phase differences between the IS/OS and the COST at two individual A-lines without light stimulus (see Supplementary Section 6). The STD of such phase difference was calculated to evaluate the phase stability. As shown in Fig. 6e, across the entire field of view while excluding the gaps between cones, the PRSMC method achieved higher phase stability/smaller STDs of phase fluctuation (272.2±184.0 mrad, mean±STD) than the pixel-level correction method (341.1 ± 196.1 mrad), whereas, in contrast, the FT-based correction significantly degrades the phase stability (744.2 ± 271.3 mrad). More

interestingly, in human ORG measurements with light stimulation, our PRSMC approach can also recover individual ORG signals that would be otherwise decorrelated using the pixel-level correction method (Fig. 6f). We also extracted the averaged human ORG signal using our PRSMC method, as shown in Fig. 6g.

4. Discussion

In this article, we demonstrate a phase-restoring subpixel motion correction (PRSMC) approach for post-hoc image registration in FD-OCT, which allows translational shifting of OCT images by arbitrary displacements while accurately restoring physically meaningful phase components. Comparatively, according to our study shown in this article, the previous FT-based correction method would fail to accurately restore the complex-valued OCT signal in the axially shifted FD-OCT images. We found that when imaging moving samples, the phase difference measured by an FD-OCT consists of both the expected Doppler shift that corresponds to the sample movement and a motion-induced phase error (MIPE) due to the change of the PSF weighted reflectivity of scatterers. Such a phase error can be corrected only if we can reproduce the same sampling points at each frame of the time-elapsed recording. Intriguingly, our proposed PRSMC method can shift the complex-valued OCT image as if the sample was physically moved to the original position, hence eliminating the MIPE when imaging moving samples (see Supplementary Section 7). Using the PRSMC, we achieved shot-noise limited phase sensitivity in detecting the displacement of a moving phantom. We also demonstrated that the PRSMC method can significantly improve amplitude stability and phase accuracy in detecting nanoscopic motion within moving samples, particularly for optoretinogram imaging. Moreover, compared with conventional pixel-level image correction and FT-based method, whose accuracies depend on the axial sampling rate (see Supplementary Section 8), the correction accuracy of the PRSMC is independent of the axial sampling rate given that the motion estimation is accurate.

Meanwhile, our current study still has some limitations: The residual MIPE after PRSMC mainly depends on the accuracy of translational motion estimation, which can be improved by adopting more sophisticated subpixel-level motion estimation methods based on fitting or optimization strategies [32]. For repeated B-scans, the phase error due to out-of-plane motion remained uncorrected, which can be resolved by recording volumetric scans consisting of multiple densely sampled B-scans, but at the cost of temporal resolution. For repeated volumetric scans, the bulk motion in the slow-scan dimension was still corrected at the pixel level, which may be extended to subpixel-level in future studies. Besides, the current study assumes that each B-scan is only affected by rigid translational displacement, while future research may also estimate and correct non-rigid motions [33].

Our proposed PRSMC approach has many potential applications for various OCT imaging modalities. In Doppler OCT, the phase difference between repeated or adjacent densely sampled A-scans is calculated to quantify flow velocity [2, 3, 9, 10]. However, as illustrated in this study, if the MIPE remains uncorrected, the measurement accuracy will be compromised even when the tissue moves axially by only 10 nm. In OCE, both the correlation coefficient and the Doppler shift are used to estimate sample displacements, which were derived based on the single scatterer model [12, 24, 43]. The inverse process of the proposed PRSMC method can be used for motion estimation via optimization, and the measurement accuracy can be improved by eliminating the phase error introduced by the change of local speckle patterns. In OCTA, complex-value-based algorithms possess higher motion contrast, but

their performance is susceptible to phase error due to bulk motion [44, 45], which can be well suppressed with the PRSMC method. Furthermore, our proposed approach may also be beneficial for complex-value-based averaging techniques [46] and computational adaptive optics (such as numerical refocusing [27] and aberration correction [47, 48]), where the phase stability is crucial for their implementation.

Acknowledgements

We thank G. Barbastathis at MIT, D. Palanker at Stanford University, and A. Roorda at the University of California, Berkeley for fruitful discussions and support.

T. Ling acknowledges the support of the National Research Foundation, Singapore for the NRF Fellowship Award (NRF-NRFF14-2022-0005), the Startup Grant (SUG) from Nanyang Technological University, and the seed funding programme under NMRC Centre Grant – Singapore Imaging Eye Network (SIENA) (NMRC/CG/C010A/2017).

L. Schmetterer acknowledges the funding support for the National Medical Research Council (CG/C010A/2017_SERI; OFLCG/004c/2018-00; MOH-000249-00; MOH-000647-00; MOH-001001-00; MOH-001015-00; MOH-000500-00; MOH-000707-00), National Research Foundation Singapore (NRF2019-THE002-0006 and NRF-CRP24-2020-0001), A*STAR (A20H4b0141), the Singapore Eye Research Institute & Nanyang Technological University (SERI-NTU Advanced Ocular Engineering (STANCE) Program), and the SERI-Lee Foundation (LF1019-1) Singapore.

V. A. Barathi acknowledges the support for Singapore NMRC Centre Grant (NMRC/CG/M010/2017/Pre-Clinical).

R. Sabesan and V. P. Pandiyan acknowledge the funding support for NIH/NEI grants U01EY032055, R01EY029710; Unrestricted grant from Research to Prevent Blindness to UW Ophthalmology, Burroughs Wellcome Fund Careers at the Scientific Interfaces Award.

Author contributions

H.L. and T.L. conceived and designed the study. B.T., V.P.P., R.S., and L.S. built the setup. H.L., B.T., and V.P.P. conducted the experiments. H.L. and T.L. analyzed the data. V.A.B. supported the animal experiments. H.L. and T.L. wrote the manuscript. All work was supervised by T.L.

Conflict of interest

H.L. and T.L. are inventors on pending patent applications related to this work filed by Nanyang Technological University (Singapore provisional patent application no. 10202204323S, filed 25 April 2022).

V.P.P. and R.S. have a commercial interest in a US patent (PCT/US2020/029984) describing the technology for the line-scan OCT for optoretinography.

Data availability

All data needed to evaluate the conclusions in the paper are present in the paper and/or the Supplementary Materials. Additional data related to this paper may be requested from the authors.

References

1. R. Leitgeb, C. Hitzenberger, and A. Fercher, "Performance of fourier domain vs. time domain optical coherence tomography," Opt Express **11**, 889-894 (2003).
2. Z. Chen, T. E. Milner, S. Srinivas, X. Wang, A. Malekafzali, M. J. C. van Gemert, and J. S. Nelson, "Noninvasive imaging of in vivo blood flow velocity using optical Doppler tomography," Optics Letters **22**, 1119-1121 (1997).
3. J. A. Izatt, M. D. Kulkarni, S. Yazdanfar, J. K. Barton, and A. J. Welch, "In vivo bidirectional color Doppler flow imaging of picoliter blood volumes using optical coherence tomography," Optics Letters **22**, 1439-1441 (1997).
4. B. Braaf, K. A. Vermeer, K. V. Vienola, and J. F. de Boer, "Angiography of the retina and the choroid with phase-resolved OCT using interval-optimized backstitched B-scans," Optics Express **20**, 20516-20534 (2012).
5. B. F. Kennedy, S. H. Koh, R. A. McLaughlin, K. M. Kennedy, P. R. T. Munro, and D. D. Sampson, "Strain estimation in phase-sensitive optical coherence elastography," Biomedical Optics Express **3**, 1865-1879 (2012).
6. F. K. Brendan, M. Francisco Gomes, C. Lixin, and D. S. David, "Three-dimensional optical coherence elastography by phase-sensitive comparison of C-scans," Journal of Biomedical Optics **19**, 1-7 (2014).
7. M. Sticker, C. K. Hitzenberger, R. Leitgeb, and A. F. Fercher, "Quantitative differential phase measurement and imaging in transparent and turbid media by optical coherence tomography," Optics Letters **26**, 518-520 (2001).
8. S. Makita, F. Jaillon, I. Jahan, and Y. Yasuno, "Noise statistics of phase-resolved optical coherence tomography imaging: single-and dual-beam-scan Doppler optical coherence tomography," Optics Express **22**, 4830-4848 (2014).
9. V. J. Srinivasan, S. Sakadžić, I. Gorczynska, S. Ruvinskaya, W. Wu, J. G. Fujimoto, and D. A. Boas, "Quantitative cerebral blood flow with Optical Coherence Tomography," Optics Express **18**, 2477-2494 (2010).
10. Y. Zhao, Z. Chen, C. Saxer, S. Xiang, J. F. de Boer, and J. S. Nelson, "Phase-resolved optical coherence tomography and optical Doppler tomography for imaging blood flow in human skin with fast scanning speed and high velocity sensitivity," Opt Lett **25**, 114-116 (2000).
11. R. K. Wang, Z. Ma, and S. J. Kirkpatrick, "Tissue Doppler optical coherence elastography for real time strain rate and strain mapping of soft tissue," Applied Physics Letters **89**, 144103 (2006).
12. K. V. Larin, and D. D. Sampson, "Optical coherence elastography - OCT at work in tissue biomechanics [Invited]," Biomedical Optics Express **8**, 1172-1202 (2017).
13. V. P. Pandiyan, A. Maloney-Bertelli, J. A. Kuchenbecker, K. C. Boyle, T. Ling, Z. C. Chen, B. H. Park, A. Roorda, D. Palanker, and R. Sabesan, "The optoretinogram reveals the primary steps of

phototransduction in the living human eye," Science Advances **6**, eabc1124 (2020).

14. F. Zhang, K. Kurokawa, A. Lassoued, J. A. Crowell, and D. T. Miller, "Cone photoreceptor classification in the living human eye from photostimulation-induced phase dynamics," Proc Natl Acad Sci U S A **116**, 7951-7956 (2019).
15. D. Hillmann, H. Spahr, C. Pfaffle, H. Sudkamp, G. Franke, and G. Huttmann, "In vivo optical imaging of physiological responses to photostimulation in human photoreceptors," Proc Natl Acad Sci U S A **113**, 13138-13143 (2016).
16. V. P. Pandiyan, X. Jiang, A. Maloney-Bertelli, J. A. Kuchenbecker, U. Sharma, and R. Sabesan, "High-speed adaptive optics line-scan OCT for cellular-resolution optoretinography," Biomedical Optics Express **11**, 5274-5296 (2020).
17. G. Goetz, T. Ling, T. Gupta, S. Kang, J. Wang, P. D. Gregory, B. H. Park, and D. Palanker, "Interferometric mapping of material properties using thermal perturbation," Proceedings of the National Academy of Sciences **115**, E2499-E2508 (2018).
18. D. Veysset, T. Ling, Y. Zhuo, V. P. Pandiyan, R. Sabesan, and D. Palanker, "Interferometric imaging of thermal expansion for temperature control in retinal laser therapy," Biomed. Opt. Express **13**, 728-743 (2022).
19. M. S. Hepburn, K. Y. Foo, P. Wijesinghe, P. R. T. Munro, L. Chin, and B. F. Kennedy, "Speckle-dependent accuracy in phase-sensitive optical coherence tomography," Opt Express **29**, 16950-16968 (2021).
20. B. Braaf, K. V. Vienola, C. K. Sheehy, Q. Yang, K. A. Vermeer, P. Tiruveedhula, D. W. Arathorn, A. Roorda, and J. F. de Boer, "Real-time eye motion correction in phase-resolved OCT angiography with tracking SLO," Biomedical Optics Express **4**, 51-65 (2013).
21. B. J. Vakoc, G. J. Tearney, and B. E. Bouma, "Statistical properties of phase-decorrelation in phase-resolved Doppler optical coherence tomography," IEEE Trans Med Imaging **28**, 814-821 (2009).
22. B. Hyle Park, M. C. Pierce, B. Cense, S.-H. Yun, M. Mujat, G. J. Tearney, B. E. Bouma, and J. F. d. Boer, "Real-time fiber-based multi-functional spectral-domain optical coherence tomography at 1.3 µm," Optics Express **13**, 3931-3944 (2005).
23. R. K. Wang, and Z. Ma, "Real-time flow imaging by removing texture pattern artifacts in spectral-domain optical Doppler tomography," Optics Letters **31**, 3001-3003 (2006).
24. K. Kurokawa, S. Makita, Y.-J. Hong, and Y. Yasuno, "Two-dimensional micro-displacement measurement for laser coagulation using optical coherence tomography," Biomedical Optics Express **6**, 170-190 (2015).
25. J. Kalkman, "Fourier-Domain Optical Coherence Tomography Signal Analysis and Numerical Modeling," International Journal of Optics **2017**, 1-16 (2017).
26. S. Y. Ksenofontov, P. A. Shilyagin, D. A. Terpelov, V. M. Gelikonov, and G. V. Gelikonov, "Numerical method for axial motion artifact correction in retinal spectral-domain optical coherence tomography," Frontiers of Optoelectronics **13**, 393-401 (2019).
27. K. Oikawa, D. Oida, S. Makita, and Y. Yasuno, "Bulk-phase-error correction for phase-sensitive signal processing of optical coherence tomography," Biomedical Optics Express **11**, 5886-5902 (2020).
28. J. Lee, V. Srinivasan, H. Radhakrishnan, and D. A. Boas, "Motion correction for phase-resolved dynamic optical coherence tomography imaging of rodent cerebral cortex," Optics express **19**,

21258-21270 (2011).

29. L. Guo, P. Li, C. Pan, R. Liao, Y. Cheng, W. Hu, Z. Chen, Z. Ding, and P. Li, "Improved motion contrast and processing efficiency in OCT angiography using complex-correlation algorithm," Journal of Optics **18**, 025301 (2016).
30. J. Y. Fan, Y. He, P. H. Wang, G. X. Liu, and G. H. Shi, "Interplane bulk motion analysis and removal based on normalized cross-correlation in optical coherence tomography angiography," Journal of Biophotonics **13** (2020).
31. M. Guizar-Sicairos, S. T. Thurman, and J. R. Fienup, "Efficient subpixel image registration algorithms," Optics letters **33**, 156-158 (2008).
32. X. Tong, Z. Ye, Y. Xu, S. Gao, H. Xie, Q. Du, S. Liu, X. Xu, S. Liu, K. Luan, and U. Stilla, "Image Registration With Fourier-Based Image Correlation: A Comprehensive Review of Developments and Applications," IEEE Journal of Selected Topics in Applied Earth Observations and Remote Sensing **12**, 4062-4081 (2019).
33. L. Pan, and X. Chen, "Retinal OCT Image Registration: Methods and Applications," IEEE Rev Biomed Eng **PP** (2021).
34. N. H. Do, "Parallel processing for adaptive optics optical coherence tomography (AO-OCT) image registration using GPU," (2016).
35. Z. Li, V. P. Pandiyan, A. Maloney-Bertelli, X. Jiang, X. Li, and R. Sabesan, "Correcting intra-volume distortion for AO-OCT using 3D correlation based registration," Opt Express **28**, 38390-38409 (2020).
36. V. Rasche, R. Proksa, R. Sinkus, P. Bornert, and H. Eggers, "Resampling of data between arbitrary grids using convolution interpolation," IEEE transactions on medical imaging **18**, 385-392 (1999).
37. P. L. Reu, "Experimental and numerical methods for exact subpixel shifting," Experimental mechanics **51**, 443-452 (2011).
38. V. Y. Zaitsev, L. Matveev, A. Matveyev, G. Gelikonov, and V. Gelikonov, "A model for simulating speckle-pattern evolution based on close to reality procedures used in spectral-domain OCT," Laser Physics Letters **11**, 105601 (2014).
39. B. Tan, Z. Hosseinaee, L. Han, O. Kralj, L. Sorbara, and K. Bizheva, "250 kHz, 1.5 µm resolution SD-OCT for in-vivo cellular imaging of the human cornea," Biomedical Optics Express **9**, 6569-6583 (2018).
40. A. Hughes, "A schematic eye for the rat," Vision research **19**, 569-588 (1979).
41. S. J. Chiu, X. T. Li, P. Nicholas, C. A. Toth, J. A. Izatt, and S. Farsiu, "Automatic segmentation of seven retinal layers in SDOCT images congruent with expert manual segmentation," Optics Express **18**, 19413-19428 (2010).
42. Y. Zhang, H. Li, T. Cao, R. Chen, H. Qiu, Y. Gu, and P. Li, "Automatic 3D adaptive vessel segmentation based on linear relationship between intensity and complex-decorrelation in optical coherence tomography angiography," Quant Imaging Med Surg **11**, 895-906 (2021).
43. J. M. Schmitt, "OCT elastography: imaging microscopic deformation and strain of tissue," Optics Express **3**, 199-211 (1998).
44. H. Li, K. Liu, L. Yao, X. Deng, Z. Zhang, and P. Li, "ID-OCTA: OCT angiography based on inverse SNR

and decorrelation features," Journal of Innovative Optical Health Sciences **14**, 2130001 (2021).

45. J. Xu, S. Song, Y. Li, and R. K. Wang, "Complex-based OCT angiography algorithm recovers microvascular information better than amplitude- or phase-based algorithms in phase-stable systems," Phys Med Biol **63**, 015023 (2017).
46. M. Szkulmowski, and M. Wojtkowski, "Averaging techniques for OCT imaging," Optics Express **21**, 9757-9773 (2013).
47. D. Hillmann, H. Spahr, C. Hain, H. Sudkamp, G. Franke, C. Pfäffle, C. Winter, and G. Hüttmann, "Aberration-free volumetric high-speed imaging of in vivo retina," Scientific Reports **6**, 35209 (2016).
48. S. G. Adie, B. W. Graf, A. Ahmad, P. S. Carney, and S. A. Boppart, "Computational adaptive optics for broadband optical interferometric tomography of biological tissue," Proceedings of the National Academy of Sciences **109**, 7175-7180 (2012).